ARTICLE

Graphene Oxide–MnO_2 Nanocomposites for Supercapacitors

Sheng Chen, Junwu Zhu,* Xiaodong Wu, Qiaofeng Han, and Xin Wang*

Key Laboratory for Soft Chemistry and Functional Materials (Nanjing University of Science and Technology), Ministry of Education, Nanjing 210094, China

ABSTRACT A composite of graphene oxide supported by needle-like MnO_2 nanocrystals (GO–MnO_2 nanocomposites) has been fabricated through a simple soft chemical route in a water–isopropyl alcohol system. The formation mechanism of these intriguing nanocomposites investigated by transmission electron microscopy and Raman and ultraviolet–visible absorption spectroscopy is proposed as intercalation and adsorption of manganese ions onto the GO sheets, followed by the nucleation and growth of the crystal species in a double solvent system *via* dissolution–crystallization and oriented attachment mechanisms, which in turn results in the exfoliation of GO sheets. Interestingly, it was found that the electrochemical performance of as-prepared nanocomposites could be enhanced by the chemical interaction between GO and MnO_2. This method provides a facile and straightforward approach to deposit MnO_2 nanoparticles onto the graphene oxide sheets (single layer of graphite oxide) and may be readily extended to the preparation of other classes of hybrids based on GO sheets for technological applications.

KEYWORDS: MnO_2 nanocrystals · hybrid material · graphene oxide · supercapacitors · capacitance

Over the past few years, considerable effort has been devoted to the development of alternative energy storage/conversion devices with high power and energy densities because of the ever-increasing environmental problems and the up-coming depletion of fossil fuels.[1–3] As an intermediate system between dielectric capacitors and batteries, supercapacitors have attracted a great deal of attention owing to their higher power densities relative to secondary batteries and traditional electric double-layer capacitors.[4,5]

The research on carbon nanotubes (CNTs) has drawn great attention because of their widespread applications in fields such as catalysts, sensors, supercapacitors, and so on.[6] Recently the study of graphenes became another hot topic owing to their monolayer arrangement of carbon atoms in a honeycomb network, which can be considered as an unrolled CNT.[7–9] Graphene oxide (GO), one of the most important derivatives of graphene, is characterized by a layered structure with oxygen functional groups bearing on the basal planes and edges.[10–13] The utilization of various carbonaceous material, such as activated carbons, carbon fibers, and CNTs, as the electrode materials for supercapacitors has been investigated extensively.[14–17] However, to our best knowledge, little work has been carried out on the application of GOs in supercapacitors.[18–20]

Manganese dioxide (MnO_2) is one of the most stable manganese oxides with excellent physical and chemical properties under ambient conditions.[21–24] In particular the rich polymorphism and structural flexibility of these compounds have allowed them a wide range of applications including catalysis, biosensors, energy storage, and so on.[25,26] As a potentially excellent electrode material for the replacement of RuO_2 in supercapacitors, MnO_2 electrodes have exhibited distinguished properties owing to their high specific capacitance, environmental compatibility, and cost effectiveness.[27–30]

Generally, there are two types of supercapacitors based on the electrode materials: (1) high surface area, inert and conductive materials that store and release energy by nanoscopic charge separation at the electrochemical interface between an electrode and an electrolyte and (2) some redox active materials that use fast, reversible redox reactions at the surface of active materials, which is known as the pseudocapacitance.[5,31–33] The carbonaceous nanostructures (like CNTs, active carbon, and graphene) are commonly studied as electrodes for electrochemical double layer capacitors (EDLCs); while transition metal oxides, including MnO_2, are promising material for pseudocapacitors.

*Address correspondence to wxin@public1.ptt.js.cn, zhujw@mail.njust.edu.cn.

Received for review September 28, 2009 and accepted March 31, 2010.

Published online April 12, 2010.
10.1021/nn901311t

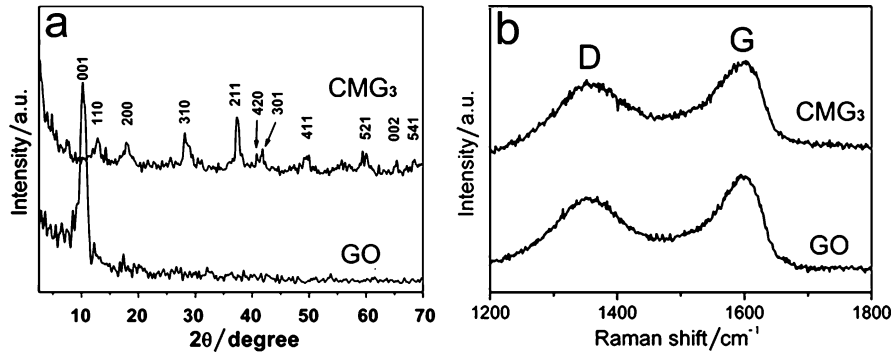

Figure 1. (a) XRD patterns (b) Raman spectra of GO and CMG_3.

Herein, we present an approach of using GO−MnO_2 nanocomposites as electrode material for supercapacitors. To the best of our knowledge, few studies on the preparation of GO−MnO_2 nanocomposites have been reported so far. The electrochemical properties of as-obtained nanocomposites with different mass ratios were investigated, together with their individual components (nano-MnO_2 and GO) and bulk MnO_2 for comparison. Moreover, the possible formation mechanism of these nanocomposites was derived. Most importantly, our experiments suggest that the application of the double solvent system plays a significant role in anchoring needle-like MnO_2 onto GO sheets and that the growth of these crystals in turn is of great benefit to further exfoliating GO.

RESULTS AND DISCUSSION

Typical XRD patterns and Raman spectra of GO and CMG_3 (chemically synthesized GO−MnO_2 nanocomposites when the feeding ratio of MnO_2/GO is 3/1; the mass of MnO_2 is calculated by $MnCl_2$ according to the reaction: $2KMnO_4 + 3MnCl_2 + 2H_2O \rightarrow 5MnO_2 + 2KCl + 4HCl$) are presented in Figure 1. The spectral features of nanocomposites with other feeding ratios are similar. As displayed in Figure 1a, the most intensive peak of GO at around $2\theta = 10.2°$ corresponds to the (001) reflection, and the interlayer spacing (0.87 nm) was much larger than that of pristine graphite (0.34 nm) due to the introduction of oxygen-containing functional groups on the graphite sheets.[34] The diffraction peaks of as-synthesized CMG_3 are similar to those of a nanotetragonal phase of α-MnO_2 (JCPDS 44-0141, a = 9.7845 Å, c = 2.8630 Å), where the (001) reflection peak of layered GO has almost disappeared. Our results correlate well with the previous studies that the diffraction peaks become weakened or even disappear whenever the regular stacks of GO are exfoliated.[35] Moreover, there are seldom differences between GO and CMG_3 from the Raman spectra in the range of 1200−1800 cm^{-1} (Figure 1b), indicating that GO was not reduced under the applied conditions and existed as a component of CMG_3. This conclusion is also supported by the results from XRD, Raman, and FTIR spectroscopies of GO and GOI (GO treated with isopropyl alcohol, see Methods) in Figure 1S (Supporting Information). Thus it is safe for us to derive that GO with its destroyed layered structure and α-MnO_2 in a tetragonal phase coexist in the prepared nanocomposites.

The heterostructure of these nanocomposites can be verified by morphological analyses. Figure 2a reveals that GO sheets are multilayers with diameters of a few micrometers, while nano-MnO_2 (Figure 2b) shows needle-like morphology with typical diameters of 20−50 nm and lengths of 200−500 nm. Figure 2 c−f is the representative TEM images of as-synthesized nanocomposites (take CMG_3 for example). It can be

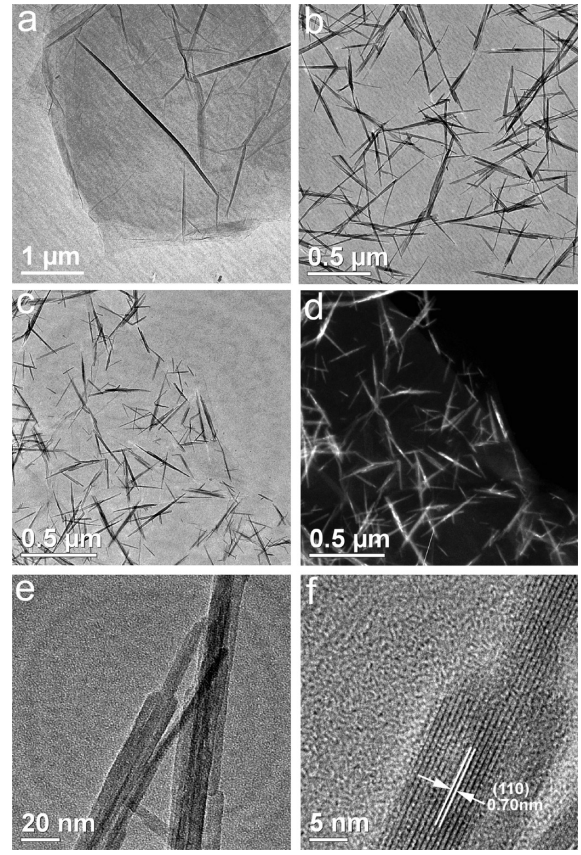

Figure 2. (a, b) TEM images of GO and nano-MnO_2; (c, d) bright-field and dark-field images of CMG_3; (e, f) the HRTEM images of a MnO_2 nanoneedle.

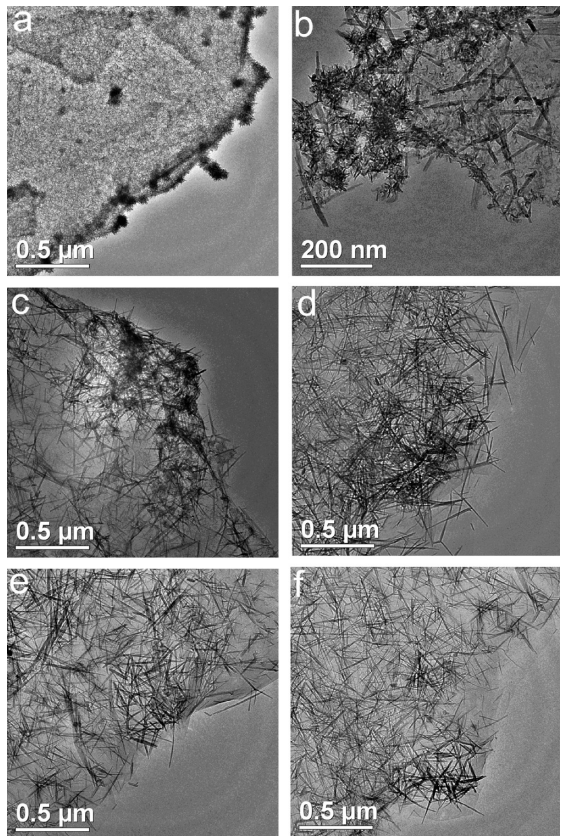

Figure 3. TEM images of CMG_3 samples collected at different time intervals: (a) 10 s, (b) 1 min, (c) 3 min, (d) 5 min, (e) 10 min, (f) 30 min.

clearly seen from Figure 2c that the GO sheets have been exfoliated and decorated randomly with the MnO_2 nanoneedles; consistent with the XRD observations. Interestingly, no obvious difference in the morphology of MnO_2 in Figure 2b and c suggests a similar growth process for the crystals on and out of the GO supports. Comparing the bright-field and dark-field TEM images in Figure 2c,d, the single layered graphene oxide sheet can be clearly distinguished from the background. Remarkably, we find that some MnO_2 nanoneedles are brighter than others which seem to be enveloped by a thin film. Since the functional groups, such as hydroxyl and epoxy groups, are attached to both sides of GO sheets, the MnO_2 nanoneedles appear on both side of the support: some locate above the graphene oxide sheet, while others lie the back of the sheet.[36]

The tip of a MnO_2 nanoneedle is shown in Figure 2e,f. It can be clearly seen from Figure 2e that the nanoneedle is actually composed of a few primary nanorods aggregated along the lateral faces. The nanorods of the center portions are longer than others, giving an indication that the oriented attachment mechanism played an important role in the formation of the nanoneedles.[37] Additionally, the lattice fringes with interplanar distances of approximately 0.7 nm shown in Figure 2f correspond to the (110) plane of the tetragonal α-MnO_2 structure, which is consistent with XRD results.[37,38] All our experiments confirm unambiguously that α-MnO_2 nanoneedles have been successfully attached onto the exfoliated GO sheets.

To investigate the formation process of the GO−MnO_2 nanocomposites, some samples of CMG_3 were taken directly from the reaction mixture at different time intervals, and analyzed by TEM, UV−vis, and Raman measurements. As displayed in Figure 3a, the samples, with a time duration of 10 s, were GO sheets with disordered precursors on their surfaces. Figure 3b−e show TEM images of CMG_3 samples with the reaction proceeding from 1 to 10 min; the less ordered precursors on the GO sheets gradually disappeared with the emergence of more nanoneedles *via* a dissolution−crystallization mechanism. The morphology for samples (Figure 3f) with a longer reaction time of 30 min displayed no pronounced distinction, suggesting the crystal growth process was almost completed after a reaction time of 10 min.

This conclusion can also be supported by UV−vis and Raman spectroscopies. As observed in Figure 4, the UV−vis absorption peak of MnO_2 gradually redshifted from 413.0 to 436.1 nm (corresponding to d−d transitions of Mn ions in MnO_2 nanocrystals[39]) when the reaction proceeded from 10 s to 10 min, due to the increased particle sizes of MnO_2,[40,41] whereas the absorption peak of GO centered at 234.1 nm (corresponding to $\pi \rightarrow \pi^*$ transitions of aromatic C−C bonds[42]) gradually blueshifted to 216.5 nm simultaneously, which can be attributed to the exfoliation of layered GO sheets within the duration.[41] Raman spectra of the CMG_3 samples collected at different time intervals are shown in Figure 5. Commonly, the Raman peak area is quantitatively related to the concentration of the particular species.[13] It can be clearly seen from Figure 5a that there are two diagnostic peaks of GO centered around 1360 and 1600 cm^{-1}, corresponding to the breathing mode of κ-point phonons of A_{1g} symmetry and the

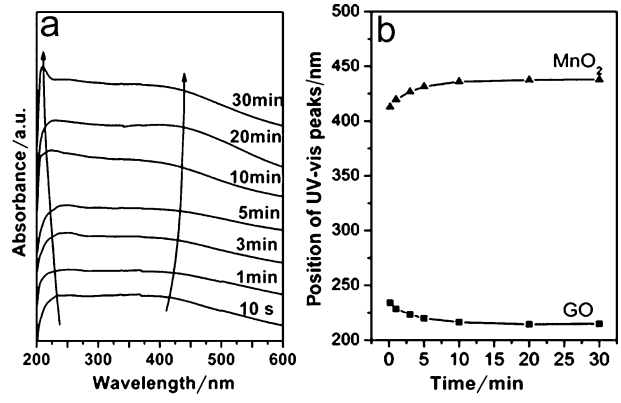

Figure 4. (a) UV−vis spectra of CMG_3 samples collected at different time intervals; (b) plot of UV−vis peak position of CMG_3 samples as a function of reaction time.

first-order scattering of the E_{2g} phonons, respectively.[43] The sharp peak around 640 cm^{-1}, labeled as C, is assigned to the Mn−O vibrations perpendicular to the direction of the MnO_6 octahedral double chains of MnO_2.[39] So the C/(D+G) peak area ratio can be employed here to reveal the proportion of MnO_2/GO in the nanocomposites. The plot of the C/(D+G) peak area ratio as a function of reaction time of CMG_3 is displayed in Figure 5b; the value increases from 0.36 to 0.69 when the reaction time increases from 10 s to 10 min, suggesting the growth of crystal species to form MnO_2 nanocrystals within that period. The variation in intensity might be attributed to the different microscopic areas selected for Raman detection. Moreover, negligible differences observed in both UV−vis and Raman spectra after 10 min provide more evidence for the completeness of the reaction,[44] strengthened the TEM observations. This phenomenon is slightly different from our previous studies when in the absence of GO, nano-MnO_2 with needle-like shapes formed in only about 5 min.[40] Therefore, GO is speculated to be a retardant in the growth of MnO_2 nanocrystals.

On the basis of our experimental results, a mechanism to interpret the formation of as-obtained GO−MnO_2 nanocomposites is put forward, as shown in Scheme 1. As shown by previous studies, GO sheets have their basal planes decorated mostly with epoxy and hydroxyl groups, while carbonyl and carboxyl groups are located at the edges. These functional groups, acting as anchor sites, enable the subsequent *in situ* formation of nanostructures attaching on the surfaces and edges of GO sheets.[36] The structural framework of MnO_2 is made of basic MnO_6 octahedron units, which are linked in different ways to produce MnO_2 crystals with different crystallographic forms and morphologies.[28,37]

At the initial stage, Mn^{2+} ions, formed by the dissolution of $MnCl_2 \cdot 4H_2O$ in isopropyl alcohol, favorably bind with the O atoms of the negatively charged oxygen-containing functional groups on GO sheets *via* an electrostatic force. With the addition of a solution of $KMnO_4$ at a relatively higher temperature (approximately 83 °C), a large number of nuclei were formed in a short time from the redox reaction occurring between Mn^{2+} and Mn^{7+}. The Mn atoms of the MnO_6 octahedron may form bonds with O atoms of the functional groups *via* an intermolecular hydrogen bond or a covalent coordination bond, acting as anchor sites for the crystals to grow.

In the case of the formation of needle-like MnO_2, our previous study provides a reasonable interpretation for this phenomenon.[40] Specifically, the ratio of DI-water/isopropyl alcohol and the manner of adding the $KMnO_4$ solution play an important role in governing the morphology of the prepared products. It is documented that the (001) faces of MnO_2

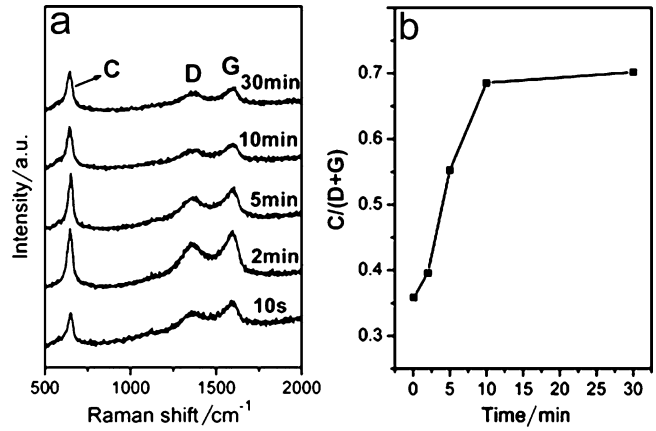

Figure 5. (a) Raman spectra of CMG_3 samples collected at different time intervals; (b) plot of C/(D+G) peak area ratio of CMG_3 samples as a function of reaction time.

crystals are the most energetic ones,[37] and that H_2O molecules coordinate with MnO_6 octahedron units more easily than isopropyl alcohol due to the polarity, steric hindrance, electrostatic effect, *etc.*[45] Therefore, H_2O molecules will interact with the O atoms of MnO_6 units in the (001) direction in priority. With the addition of a smaller amount of water (H_2O/isopropyl alcohol = 5:50 mL), thermodynamically only O atoms along the (001) direction would bind with H_2O molecules, whereas the ones in other directions would coordinate with isopropyl alcohol.

It should be noted that the coordination of H_2O and isopropyl alcohol with the O atoms of MnO_6 has a discrepant effect on the packing of the crystal growing species. The intermolecular hydrogen bonds formed among the H_2O coordinated species make the species favorable to form highly ordered aggregates; whereas a shortage of such strong intermolecular interactions in isopropyl alcohol coordinated species leads the crystal stacking to be disordered. As a result, the overall system had only one preferable crystal growth direction, for the case with less water (5 mL) employed, yielding MnO_2 with a 1D nanostructure.

Significantly, the manner of adding $KMnO_4$ solution exerts an influence on the formation and stacking of the nuclei in the crystal growth process. A rapid introduction of $KMnO_4$ solution causes the formation of a large amount of growing species in a short time. Dissolution−crystallization and oriented attachment are two simultaneous processes in crystal growth,[37] and kinetically, the center of the primary nanorod has a higher growing speed compared with the other directions, thus needle-like products are produced in the end.

Moreover, as indicated by the results of UV−vis measurements, the exfoliation of GO sheets and the growth of crystals are two simultaneous processes. Thus, the growth of *in situ* formed crystals may also in turn contribute to the destruction of regular layered GO

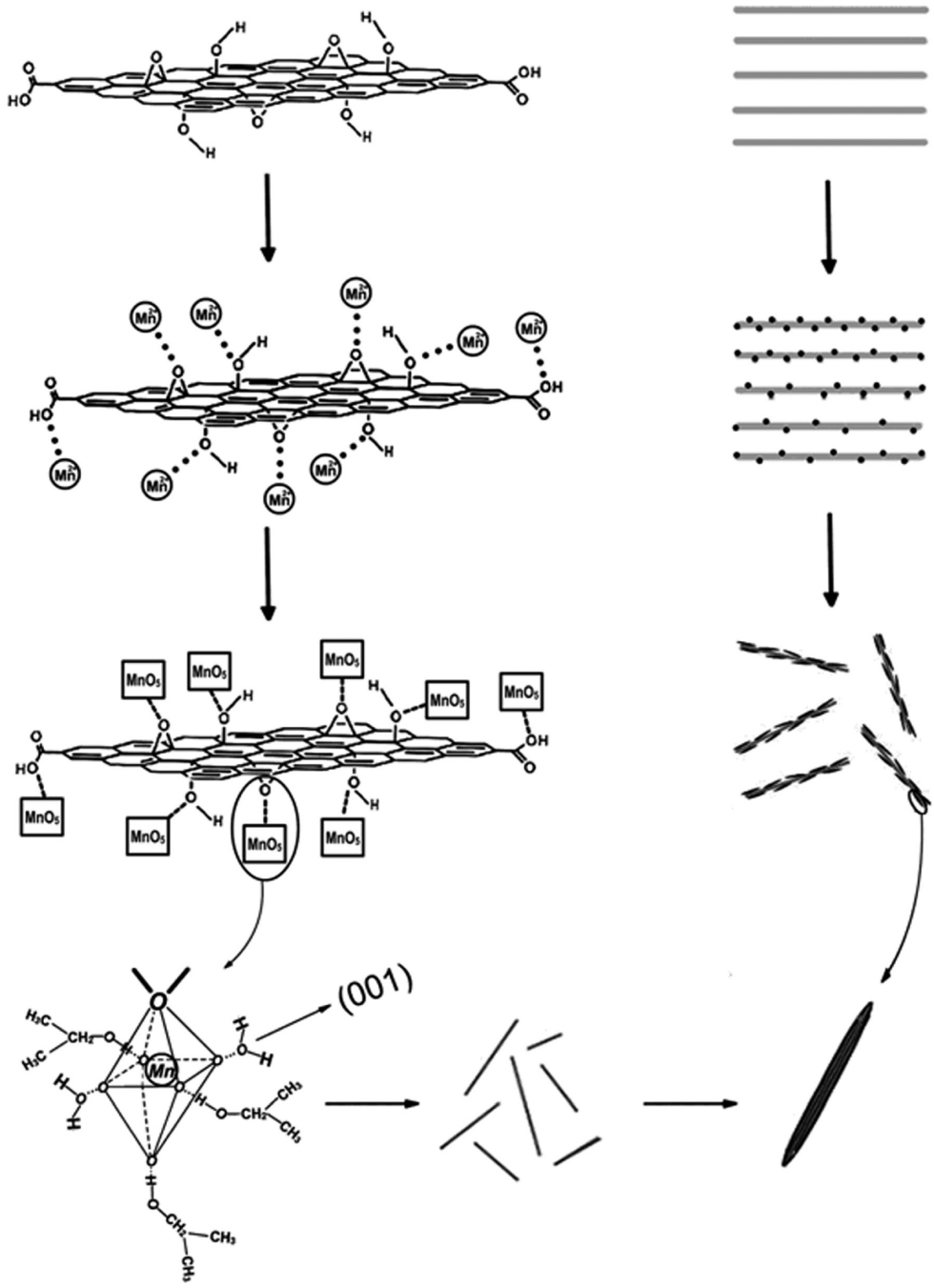

Scheme 1. The formation mechanism for GO−MnO_2 nanocomposites.

sheets and the formation of exfoliated graphene oxide.[36]

Furthermore, as reported by previous studies, $KMnO_4$ can also react with carbonaceous materials, such as CNTs, active carbon, *etc*, forming manganese oxide−carbon composites.[46−48] Thus controlled experiments using only GO and $KMnO_4$ as the precursors *via* a similar procedure were conducted. But few MnO_2 nanoneedles can be observed (Figure 2S, Supporting Information). On the other hand, nano-MnO_2 synthesized chemically in the absence of GO *via* a similar procedure shows a needle-like morphology (Figure 2b). So it is speculated that the formation of needle-like MnO_2 may be attributable to the direct reaction between $MnCl_2 \cdot 4H_2O$ and $KMnO_4$ in the water−isopropyl alcohol system as reported by our previous study.[40] Further studies on the growth mechanism and the effects of other reaction parameters (such as solvents, manganese precursors, concentrations, reaction time, and pH) are still in progress.

To explore the potential applications of as-synthesized nanocomposites, the samples were fabricated into supercapacitor electrodes and characterized with cyclic voltammograms (CVs) and galvanostatic

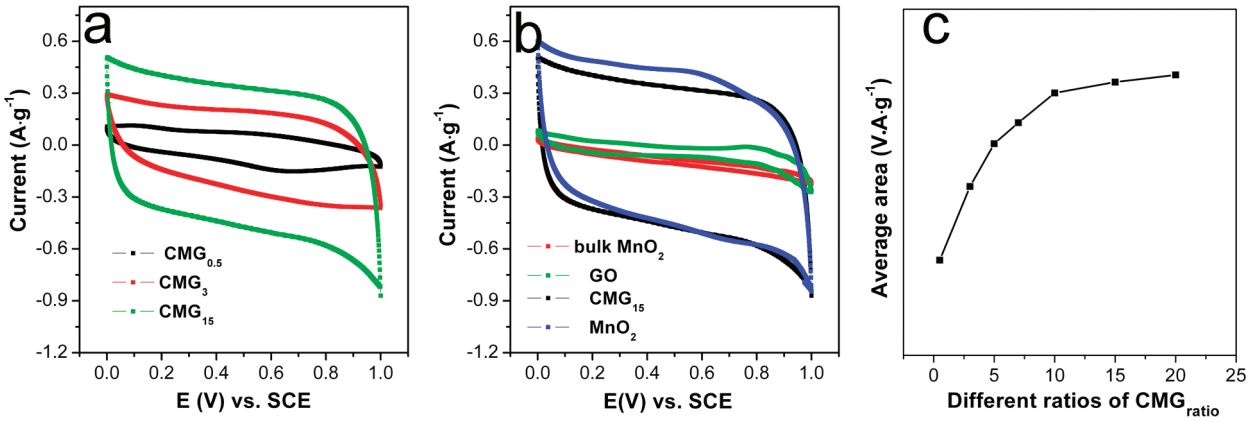

Figure 6. CVs of (a) $CMG_{0.5}$, CMG_3, CMG_{15}; (b) bulk MnO_2, GO, CMG_{15}, and nano-MnO_2 at 5 mV · s^{-1} in 1 M Na_2SO_4 solution; (c) plot of average area of CV curves as a function of different ratios of CMG_{ratio}.

charge/discharge measurements. CV response of as-synthesized samples carried out at a scan rate of 5 mV · s^{-1} in the potential range of 0−1 V using 1 M Na_2SO_4 aqueous electrolyte solution is shown in Figure 6. The rectangular and symmetric CV curves of nano-MnO_2 indicate the ideal pseudocapacitive nature of the fabricated electrode, while the lack of symmetry in $CMG_{0.5}$, CMG_3, and CMG_{15} is probably due to combined double-layer and pseudocapacitive contribution to the total capacitance.[49] Interestingly, with the feeding ratio of MnO_2/GO increasing from 0.5 to 15, CV plots of CMG_{ratio} became more close to that of the nano-MnO_2 (Figure 6a), which can be attributed to the incremental pseudocapacitive contribution to the overall capacitance.

Moreover, the average areas of CV curves of these samples were calculated. Since C_s is proportional to the average areas of CVs,[50] the results shown in Figure 6c indicate that C_s of CMG_{ratio} increases with the ratio of MnO_2/GO from 0.5 to 10. Nevertheless, no obvious difference can be founded when the ratio is higher than 10, such as CMG_{10}, CMG_{15}, and CMG_{20} (not shown), suggesting they have nearly the same value of C_s.

Of note is that C_s of the nano-MnO_2 is much higher than that of its bulk counterpart, probably owing to the shape- and size-dependent properties appearing on the nanoscale. As reported by Devaraj *et al.*,[28] two factors are thought to make contributions to the high C_s: (1) higher specific area of nanoscale MnO_2 over the bulk one and (2) good alignment of nanoneedles that can provide well-ordered tunnels, convenient for insertion/extraction of alkali cations into/from MnO_2.

To get more information about the potential of as-synthesized GO−MnO_2 nanocomposites as electrode materials for supercapacitors, galvanostatic charge/discharge measurements were carried out in 1 M Na_2SO_4 between 0 and 1 V at a current density of 200 mA · g^{-1}. As illustrated in Figure 7a, during the charging and discharging steps, the charge curve of CMG_{15} is almost symmetric to its corresponding discharge counterpart with a slight curvature, indicating the pseudocapacitive contribution along with the double layer contribution. The C_s is calculated according to $C_s = I \times \Delta t/(\Delta V \times m)$ from the discharge curves, where I is the constant discharge current, Δt is the discharge time, and ΔV is the potential drop during discharge;[4] the C_s values of

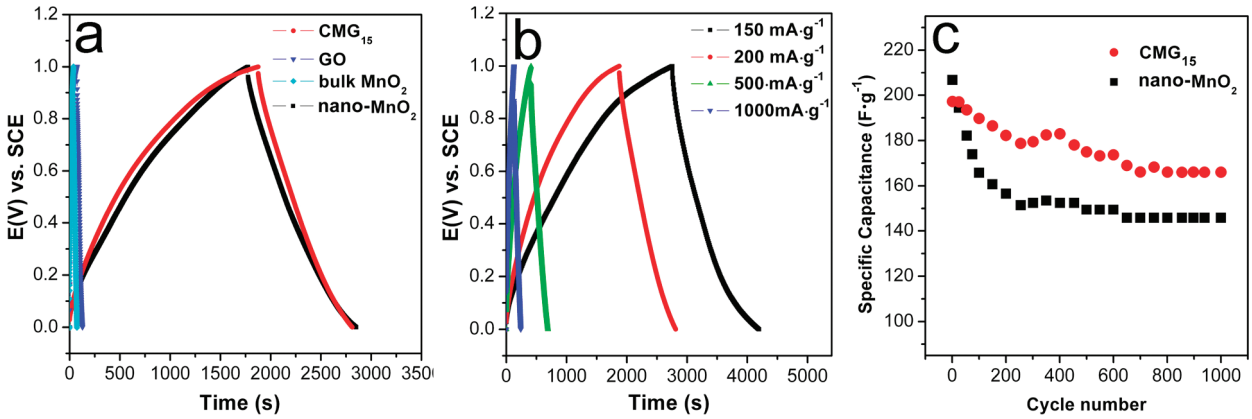

Figure 7. (a) Galvanostatic charge/discharge curves of CMG_{15}, nano-MnO_2, GO, and bulk MnO_2 at 200 mA · g^{-1}; (b) galvanostatic charge/discharge curves of CMG_{15} at 150, 200, 500, and 1000 mA · g^{-1}; (c) cycle life of CMG_{15} and nano-MnO_2 at 200 mA · g^{-1} in 1 M Na_2SO_4 solution.

CMG_{15}, nano-MnO_2, GO, and bulk MnO_2 are 197.2, 211.2, 10.9, and 6.8 $F \cdot g^{-1}$, respectively. These values are mainly consistent with the order indicated by the CVs.

Thermogravimetric analyses (TGA) was employed to determine actual content of each component in CMG_{15} (Figure 3S, Supporting Information). The experiments were performed from 50 to 700 °C at a heating rate of 20 °C $\cdot$ min^{-1} in air flow; the GO sheets were burned up while MnO_2 was turned into Mn_2O_3.[41,51] The weight loss of GO, nano-MnO_2, and CMG_{15} is found to be 88.1%, 7.2%, and 14.6%, respectively. Accordingly, the mass ratio of MnO_2/GO can be derived to be 9.8/1. Assuming proportional contributions from the components (211.2 $F \cdot g^{-1}$ of nano-MnO_2 and 10.9 $F \cdot g^{-1}$ of GO) to the overall capacitance, the C_s of the composites is derived to be 192.7 $F \cdot g^{-1}$, close to that of as-synthesized CMG_{15} (197.2 $F \cdot g^{-1}$).

On the basis of the above results, CMG_{15} was selected for further charge−discharge performance measurements. C_s calculated at 150, 200, 500, and 1000 $mA \cdot g^{-1}$ is 216.0, 197.2, 141.5, and 111.1 $F \cdot g^{-1}$, respectively (Figure 7b). About 51.4% of C_s was retained when the current density increased from 150 to 1000 $mA \cdot g^{-1}$. We ascribe this to the discrepant insertion−deinsertion behaviors of alkali ion (Na^+) from the electrolyte to MnO_2. At a low current density (150 $mA \cdot g^{-1}$), the diffusion of ions from the electrolyte can gain access to almost all available pores of the electrode, leading to a complete insertion reaction, and therefore a higher C_s. However, with the increment of current density, the effective interaction between the ions and the electrode is greatly reduced, and as a result there is a reduction in capacitance.[1]

Furthermore, the electrochemical stability of CMG_{15} and nano-MnO_2 is investigated in the range of 0−1 V at 200 $mA \cdot g^{-1}$ in 1 M Na_2SO_4 aqueous solution (Figure 7c). It is found that the CMG_{15} electrode retained about 84.1% (165.9 $F \cdot g^{-1}$) of initial capacitance after 1000 cycles, while that of the nano-MnO_2 retained only about 69.0% (145.7 $F \cdot g^{-1}$). The discrepant electrochemical stability between CMG_{15} and nano-MnO_2 may be attributable to the different double-layer and pseudocapacitive contributions. As well-known, the double-layer process only involves a charge rearrangement, while pseudocapacitive is related to a chemical reaction, and the double-layer capacitors have a better electrochemical stability but lower C_S as compared with those of pseudocapacitators.[52] Accordingly, as-synthesized CMG_{15}, making more double-layer contribution compared to that of nano-MnO_2 owning to the presence of GO, have a slightly lower C_s than the latter; however, its electrochemical stability was obviously enhanced. Although in a real capacitor, a two-electrode cell is recommended, we believe these results calculated from a three-electrode cell are still valuable for materials investigation.

Meanwhile, because graphene has a good electrochemical double layer performance in strong alkaline electrolyte solution,[20,53] further electrochemical measurements employing 6 M KOH solution as electrolyte and Hg/HgO as reference electrode were carried out to explore their electrochemical behaviors in alkaline electrolyte (Figure 4S, Supporting Information). Unfortunately, none of the CV plots could show the characteristic of a capacitor, rather than that of a battery. Nevertheless, by calculating the average area of CVs, it is interesting to find that the charge storage capacity of as-prepared samples is greatly influenced by the feeding ratios; the nanocomposites with a feeding ratio of MnO_2/GO (15:1) acquired the highest charge storage capacity, which is much higher than each individual component (nano-MnO_2 and GO), bulk MnO_2, and MMG_{15} (mechanically mixed composite with a mass ratio of MnO_2/GO (9.8/1) for the actual MnO_2/GO mass ratio of CMG_{15} is 9.8/1 as determined by TGA). The charge storage capacities of these samples quantitatively decrease in the following order: CMG_{15} > MMG_{15} > nano-MnO_2 > GO > bulk MnO_2 (Figure 4Sa−c, Supporting Information). Thus a synergistic effect is observed in this system. By comparing the TEM and FESEM images of CMG_3 and CMG_{15} (Figure 5S, Supporting Information), MnO_2 nanoneedles are found to be located in two regions, on the GO sheets and outside the supports. With an increment of the feeding ratio of MnO_2/GO from 3 to 15, more MnO_2 was anchored on the GO sheets, with more nanoneedles outside the supports. Accordingly, we speculate that the synergistic effect comprises two components, chemical binding and mechanical interactions. Since the charge storage capacity of CMG_{15} is higher than that of MMG_{15}, the decoration of MnO_2 on GO sheets, or the formation of chemical bonds between MnO_2 and GO, is speculated to play an essential role in the synergistic effect. Additionally, MMG_{15} possesses a higher charge storage capacity as compared to each individual component (nano-MnO_2 and GO), thus the scattered MnO_2 that interacts with the GO sheets *via* mechanical interaction is also speculated to contribute to the strong electrochemical behaviors of the produced nanocomposites.

It should be noted that the cycle life of MnO_2 in alkali solution can be improved by the doping of other elements like Bi, Pb, *etc.*,[54] therefore, our synthesized composites also have potential applications as the electrode material for rechargeable batteries.

CONCLUSIONS

We have demonstrated that GO−MnO_2 nanocomposites can be prepared *via* a simple solution approach at low temperature without the use of any templates or surfactants. In our procedure, an isopropyl alcohol−water solution was employed as the reacting system, which is beneficial for the oriented growth of the crystal species to form 1D MnO_2, re-

sulting in the exfoliation of GO sheets. The integration of GO and the needle-like MnO_2 crystals enables such composites to possess good electrochemical behaviors that are useful as electrode material for supercapacitors. In addition, the prepared materials are expected to have potential applications as catalysts, absorbents, and electrodes for other electronic devices.

METHODS

Synthesis of GO−MnO_2 Nanocomposites. GO was prepared from powdered flake graphite (400 mesh) by a modified Hummers method as described previously.[55,56] Nanocomposites with different feeding ratios of MnO_2/GO were synthesized. The typical route, for example, when the feeding ratio of MnO_2/GO is 3:1, is as follows: GO (0.066 g) and $MnCl_2 \cdot 4H_2O$ (0.27 g) were dispersed in isopropyl alcohol (50 mL), with ultrasonication for 0.5 h. Subsequently, the slurry was heated to approximately 83 °C in a water cooled condenser with vigorous stirring, and $KMnO_4$ (0.15 g) dissolved in 5 mL of deionized (DI) water was added rapidly into the above boiling solution. After refluxing for 0.5 h, the mixture began to cool to room temperature. The nanocomposite, labeled as CMG_{ratio} (*e.g.*, CMG_3, CMG_{15} and CMG_{20}) was then centrifuged, washed, and finally dried in air at 60 °C overnight. For comparison, nano-MnO_2 was synthesized chemically in the absence of GO *via* a similar procedure. Furthermore, to investigate the effect of isopropyl alcohol on the reduction of GO, the sample referred to as GOI (GO treated with isopropyl alcohol) was prepared without using manganese precursors and keeping the other experimental conditions unaltered. The controlled experiments using only GO and $KMnO_4$ as the precursors *via* a similar procedure were conducted to investigate the reaction between $KMnO_4$ and GO.

Characterization. Powder X-ray diffraction (XRD) analyses were performed on a Bruker D8 Advance diffractometer with Cu Kα radiation ($\lambda \approx 1.54$ Å). UV−vis absorption and/or transmission spectra were obtained using a BRAIC UV-1201 spectrophotometer. Raman spectra were run on a Renishaw Raman microscope. FT-IR spectra of KBr powder pressed pellets were recorded on a Bruker VECTOR 22 spectrometer. Thermogravimetric analyses (TGA) were performed on a TGA/SDTA851e thermogravimetric analyzer from 50 to 700 °C at a heating rate of 20 °C · min^{-1} in air flow. Morphologies of as-obtained products were observed on a transmission electron microscope (TEM, JEOL JEM-2100) and field emission scanning electron microscopy (FESEM, LEO-1550). To investigate the mechanism of the overall procedure, samples taken from the reaction mixture at different time intervals were subjected to TEM, UV−vis, and Raman analyses.

Electrochemical Measurement. The electrochemical properties of as-obtained products were investigated under a three-electrode cell configuration at room temperature. The working electrodes were fabricated by mixing the prepared powders with 15 wt % acetylene black and 5 wt % polytetrafluorene-ethylene (PTFE) binder. A small amount of DI-water was added to the mixture to produce a homogeneous paste. The mixture was pressed onto nickel foam current-collectors (1.0 cm ×1.0 cm) to make electrodes. The mass of the active material was in a range of 5.6−15.2 mg. Before the electrochemical test, the prepared electrode was soaked overnight in a 1 M Na_2SO_4 solution. Electrochemical characterization was carried out in a conventional three-electrode cell with 1 M Na_2SO_4 aqueous solution as the electrolyte. Platinum foil and a saturated calomel electrode (SCE) were used as the counter and reference electrodes, respectively. Additionally, to investigate the electrochemical behaviors of as-synthesized samples in strong alkaline solution, 1 M Na_2SO_4 was replaced by 6 M KOH as electrolyte, with the SCE replaced by Hg/HgO as reference electrode. CV measurements were conducted on a CHI 660B electrochemical workstation (Shanghai CH Instrument Company, China). The galvanostatic charge−discharge measurement was performed on a Land Battery workstation at 22 °C (Wuhan Land Instrument Company, China).

Acknowledgment. This investigation was supported by the Natural Science Foundation of China and China Academy of Engineering Physics (10776014 and 50902070), the Natural Science Foundation of Jiangsu province (No.BK2009391), and the Research Fund for the Doctoral Program of Higher Education of China (No. 20093219120011).

Supporting Information Available: XRD patterns, Raman, and FTIR spectra of GO and GOI; TEM images of as-obtained products *via* a similar procedure using only GO and $KMnO_4$ as the precursors; TG curves of GO, nano-MnO_2, and CMG_{15} at a heating rate of 20 °C · min^{-1} in air flow; CVs of $CMG_{0.5}$, CMG_3, CMG_{15}, bulk MnO_2, GO, nano-MnO_2, and MMG_{15} at 5 mV · s^{-1} in 6 M KOH solution; Plot of average area of CV curves as a function of different ratios of CMG_{ratio}; TEM and FESEM images of CMG_3 and CMG_{15}. This material is available free of charge *via* the Internet at http://pubs.acs.org.

REFERENCES AND NOTES

1. Subramanian, V.; Zhu, H.; Vajtai, R.; Ajayan, P. M.; Wei, B. Hydrothermal Synthesis and Pseudocapacitance Properties of MnO_2 Nanostructures. *J. Phys. Chem. B* **2005**, *109*, 20207–20214.
2. Mohana, A. L.; Estaline, R. F.; Imran, A.; Ramaprabhu, J. S. Asymmetric Flexible Supercapacitor Stack. *Nanoscale Res. Lett.* **2008**, *3*, 145–151.
3. A. Karina, C.-G.; Monica, L.-C.; Nieves, C.-P.; Pedro, G.-R. Nanocomposites Hybrid Molecular Materials for Application in Solid-State Electrochemical Supercapacitors. *Adv. Funct. Mater.* **2005**, *15*, 1125–1133.
4. Bao, S.-J.; Li, C. M.; Guo, C.-X.; Qiao, Y. Biomolecule-Assisted Synthesis of Cobalt Sulfide Nanowires for Application in Supercapacitors. *J. Power Sources* **2008**, *180*, 676–681.
5. Kötz, R.; Carlen, M. Principles and Applications of Electrochemical Capacitors. *Electrochim. Acta* **2000**, *45*, 2483–2496.
6. Niyogi, S.; Bekyarova, E.; Itkis, M. E.; McWilliams, J. L.; Hamon, M. A.; Haddon, R. C. Solution Properties of Graphite and Graphene. *J. Am. Chem. Soc.* **2006**, *128*, 7720–7721.
7. Tang, L.; Wang, Y.; Li, Y.; Feng, H.; Lu, J.; Li, J. Preparation, Structure, and Electrochemical Properties of Reduced Graphene Sheet Films. *Adv. Funct. Mater.* **2009**, *19*, 2782–2789.
8. Geim, A. K.; Novoselov, K. S. The Rise of Graphene. *Nature* **2007**, *6*, 183–191.
9. Shin, H., S.; Kim, K.; Benayad, A.; Yoon, S.; Park, H.; Jung, I.-S.; Jin, M.; Jeong, H.-K.; Kim, J.; Choi, J.-Y.; *et al.* Efficient Reduction of Graphite Oxide by Sodium Borohydride and Its Effect on Electrical Conductance. *Adv. Funct. Mater.* **2009**, *19*, 1987–1992.
10. He, H.; Klinowski, J.; Forster, M.; Lerf, A. A New Structural Model for Graphite Oxide. *Chem. Phys. Lett.* **1998**, *287*, 53–56.
11. Lerf, A.; He, H.; Forster, M.; Klinowski, J. Structure of Graphite Oxide Revisited. *J. Phys. Chem. B* **1998**, *102*, 4477–4482.
12. Stankovich, S.; Piner, R. D.; Nguyen, S. T.; Ruoff, R. S. Synthesis and Exfoliation of Isocyanate-Treated Graphene Oxide Nanoplatelets. *Carbon* **2006**, *44*, 3342–3347.
13. Jeong, H. K.; Lee, Y. P.; Lahaye, R. J. W. E.; Park, M. H.; An, K. H.; Kim, I. J.; Yang, C. W.; Park, C. Y.; Ruoff, R. S.; Lee, Y. H. Evidence of Graphitic AB Stacking Order of Graphite Oxides. *J. Am. Chem. Soc.* **2008**, *130*, 1362–1366.
14. Zhou, C.; Kumar, S.; Doyle, C. D.; Tour, J. M. Functionalized Single Wall Carbon Nanotubes Treated with Pyrrole for Electrochemical Supercapacitor Membranes. *Chem. Mater.* **2005**, *17*, 1997–2002.

15. Lee, J. Y.; An, K. H.; Heo, J. K.; Lee, Y. H. Fabrication of Supercapacitor Electrodes Using Fluorinated Single-Walled Carbon Nanotubes. *J. Phys. Chem. B* **2003**, *107*, 8812–8815.
16. Reddy, A. L. M.; Ramaprabhu, S. Nanocrystalline Metal Oxides Dispersed Multiwalled Carbon Nanotubes as Supercapacitor Electrodes. *J. Phys. Chem. C* **2007**, *111*, 7727–7734.
17. Kaempgen, M.; Chan, C. K.; Ma, J.; Cui, Y.; Gruner, G. Printable Thin Film Supercapacitors Using Single-Walled Carbon Nanotubes. *Nano Lett.* **2009**, *9*, 1872–1876.
18. Wang, H.; Hao, Q.; Yang, X.; Lu, L.; Wang, X. Graphene Oxide Doped Polyaniline for Supercapacitors. *Electrochem. Commun.* **2009**, *6*, 1158–1161.
19. Zhou, X.; Huang, X.; Qi, X.; Wu, S.; Xue, C.; Boey, F. Y. C.; Yan, Q.; Chen, P.; Zhang, H. *In Situ* Synthesis of Metal Nanoparticles on Single-Layer Graphene Oxide and Reduced Graphene Oxide Surfaces. *J. Phys. Chem. C* **2009**, *113*, 10842–10846.
20. Stoller, M. D.; Park, S.; Zhu, Y.; An, J.; Ruoff, R. S. Graphene-Based Ultracapacitors. *Nano Lett.* **2008**, *8*, 3498–3502.
21. Zordan, T. A.; Hepler, L. G. Thermochemistry and Oxidation Potentials of Manganese and Its Compounds. *Chem. Rev.* **1968**, *68*, 737–745.
22. Zhang, H.; Cao, G.; Wang, Z.; Yang, Y.; Shi, Z.; Gu, Z. Growth of Manganese Oxide Nanoflowers on Vertically-Aligned Carbon Nanotube Arrays for High-Rate Electrochemical Capacitive Energy Storage. *Nano Lett.* **2008**, *8*, 2664–2668.
23. Cheng, F.; Zhao, J.; Song, W.; Li, C.; Ma, H.; Chen, J.; Shen, P. Facile Controlled Synthesis of MnO_2 Nanostructures of Novel Shapes and Their Application in Batteries. *Inorg. Chem.* **2006**, *45*, 2038–2044.
24. Subramanian, V.; Zhu, H.; Wei, B. Alcohol-Assisted Room Temperature Synthesis of Different Nanostructured Manganese Oxides and Their Pseudocapacitance Properties in Neutral Electrolyte. *Chem. Phys. Lett.* **2008**, *453*, 242–249.
25. Yang, X.; Tang, W.; Feng, Q.; Ooi, K. Single Crystal Growth of Birnessite- and Hollandite-Type Manganese Oxides by a Flux Method. *Cryst. Growth Des.* **2003**, *3*, 409–415.
26. Zheng, D.; Yin, Z.; Zhang, W.; Tan, X.; Sun, S. Novel Branched γ-MnOOH and β-MnO_2 Multipod Nanostructures. *Cryst. Growth Des.* **2006**, *6*, 1733–1735.
27. Xu, M.; Kong, L.; Zhou, W.; Li, H. Hydrothermal Synthesis and Pseudocapacitance Properties of α-MnO_2 Hollow Spheres and Hollow Urchins. *J. Phys. Chem. C* **2007**, *111*, 19141–19147.
28. Devaraj, S.; Munichandraiah, N. Effect of Crystallographic Structure of MnO_2 on Its Electrochemical Capacitance Properties. *J. Phys. Chem. C* **2008**, *112*, 4406–4417.
29. Toupin, M.; Brousse, T.; Belanger, D. Influence of Microstucture on the Charge Storage Properties of Chemically Synthesized Manganese Dioxide. *Chem. Mater.* **2002**, *14*, 3946–3952.
30. Li, Q.; Olson, J. B.; Penner, R. M. Nanocrystalline α-MnO_2 Nanowires by Electrochemical Step-Edge Decoration. *Chem. Mater.* **2004**, *16*, 3402–3405.
31. An, K. H.; Kim, W. S.; Park, Y. S.; Choi, Y. C.; Lee, S. M.; Chung, D. C.; Bae, D. J.; Lim, S. C.; Lee, Y. H. Supercapacitors Using Single-Walled Carbon Nanotube Electrodes. *Adv. Mater.* **2003**, *13*, 497–500.
32. Wang, Q.; Wen, Z.; Li, J. A Hybrid Supercapacitor Fabricated with a Carbon Nanotube Cathode and a TiO_2-B Nanowire Anode. *Adv. Funct. Mater.* **2006**, *16*, 2141–2146.
33. Simon, P.; Gogotsi, Y. Materials for Electrochemical Capacitors. *Nat. Mater.* **2008**, *17*, 845–854.
34. Xu, C.; Wu, X.; Zhu, J.; Wang, X. Synthesis of Amphiphilic Graphite Oxide. *Carbon* **2007**, *46*, 386–389.
35. Xu, C.; Wang, X.; Zhu, J. Graphene and Metal Particle Nanocomposites. *J. Phys. Chem. C* **2008**, *112*, 19841–19845.
36. Xu, C.; Wang, X.; Zhu, J.; Yang, X.; Lu, L. Deposition of Co_3O_4 Nanoparticles onto Exfoliated Graphite Oxide sheets. *J. Mater. Chem.* **2008**, *18*, 5625–5629.
37. Portehault, D.; Cassaignon, S.; Baudrin, E.; Jolivet, J. P. Morphology Control of Cryptomelane Type MnO_2 Nanowires by Soft Chemistry. Growth Mechanisms in Aqueous Medium. *Chem. Mater.* **2007**, *19*, 5410–5417.
38. Villegas, J. C.; Garces, L. J.; Gomez, S.; Durand, J. P.; Suib, S. L. Particle Size Control of Cryptomelane Nanomaterials by Use of H_2O_2 in Acidic Conditions. *Chem. Mater.* **2005**, *17*, 1910–1918.
39. Gao, T.; Glerup, M.; Krumeich, F.; Nesper, R.; Fjellvåg, H.; Norby, P. Microstructures and Spectroscopic Properties of Cryptomelane-type Manganese Dioxide Nanofibers. *J. Phys. Chem. C* **2008**, *112*, 13134–13140.
40. Chen, S.; Zhu, J.; Han, Q.; Zheng, Z.; Yang, Y.; Wang, X. Shape-Controlled Synthesis of One-Dimensional MnO_2 *via* a Facile Quick-Precipitation Procedure and Its Electrochemical Properties. *Cryst. Growth Des.* **2009**, *9*, 4356–4361.
41. Ai, Z.; Zhang, L.; Kong, F.; Liu, H.; Xing, W.; Qiu, J. Microwave-Assisted Green Synthesis of MnO_2 Nanoplates with Environmental Catalytic Activity. *Mater. Chem. Phys.* **2008**, *111*, 162–167.
42. Paredes, J. I.; Villar-Rodil, S.; Martínez-A., A.; Tasco, J. M. D. Graphene Oxide Dispersions in Organic Solvents. *Langmuir* **2008**, *24*, 10560–10564.
43. Alwarappan, S.; Erdem, A.; Liu, C.; Li, C.-Z. Probing the Electrochemical Properties of Graphene Nanosheets for Biosensing Applications. *J. Phys. Chem. C* **2009**, *113*, 8853–8857.
44. Li, D.; Muller, M. B.; Gilje, S.; Kaner, R. B.; Wallace, G. G. Processable Aqueous Dispersions of Graphene Nanosheets. *Nature* **2008**, *3*, 101–105.
45. Kamlet, M. J.; Abboud, J.-L. M.; Abraham, M. H.; Taft, R. W. Linear Solvation Energy Relationships. 23. A Comprehensive Collection of the Solvatochromic Parameters, π^*, α, and 0, and Some Methods for Simplifying the Generalized Solvatochromic Equation. *J. Org. Chem.* **1983**, *48*, 2877–2887.
46. Wu, M.; Snook, G. A.; Chen, G. Z.; Fray, D. J. Redox Deposition of Manganese Oxide on Graphite for Supercapacitors. *Electrochem. Commun.* **2004**, *6*, 499–504.
47. Ma, S.-B.; Ahn, K.-Y.; Lee, E.-S.; Oh, K.-H.; Kim, K.-B. Synthesis and Characterization of Manganese Dioxide Spontaneously Coated on Carbon Nanotubes. *Carbon* **2007**, *45*, 375–382.
48. Jin, X.; Zhou, W.; Zhang, S.; Chen, G. Z. Nanoscale Microelectrochemical Cells on Carbon Nanotubes. *Small* **2007**, *3*, 1513–1517.
49. Reddy, A. L. M.; Shaijumon, M. M.; Gowda, S. R.; Ajayan, P. M. Multisegmented Au-MnO_2/Carbon Nanotube Hybrid Coaxial Arrays for High-Power Supercapacitor Applications. *J. Phys. Chem. C* **2010**, *114*, 658–663.
50. Srinivasan, V.; Weidner, J. W. Capacitance Studies of Cobalt Oxide Films Formed *via* Electrochemical Precipitation. *J. Power Sources* **2002**, *108*, 15–20.
51. Xiao, M.; Du, X.-S.; Meng, Y.-Z.; Gong, K.-C. The Influence of Thermal Treatment Conditions on the Structures and Electrical Conductivities of Graphite Oxide. *New Carbon Mater.* **2004**, *19*, 92–96.
52. Winter, M.; Brodd, R. J. What Are Batteries, Fuel Cells, and Supercapacitors. *Chem. Rev.* **2004**, *104*, 4245–4269.
53. Wang, Y.; Shi, Z.; Huang, Y.; Ma, Y.; Wang, C.; Chen, M.; Chen, Y. Supercapacitor Devices Based on Graphene Materials. *J. Phys. Chem. C* **2009**, *113*, 13103–13107.
54. Sajoj, B.; Micka, K.; Krtil, P. Study of the Rechargeable Manganese Dioxide Electrode. *Electrochim. Acta* **1995**, *40*, 2005–2011.
55. Hummers, W. S.; Offeman, R. E. Preparation of Graphitic Oxide. *J. Am. Chem. Soc.* **1958**, *80*, 1339.
56. Kovtyukhova, N. I.; Ollivier, P. J.; Martin, B. R.; Mallouk, T. E.; Chizhik, S. A.; Buzaneva, E. V.; Gorchinskiy, A. D. Layer-By-Layer Assembly of Ultrathin Composite Films from Micron-Sized Graphite Oxide Sheets and Polycations. *Chem. Mater.* **1999**, *11*, 771–778.